Two-dimensional layered SnO_2 nanosheets for ambient ammonia synthesis

Guangzhe Li†, Yaoguang Yu†, Zhefei Pan, Liang An*

Department of Mechanical Engineering, The Hong Kong Polytechnic University, Hung Hom, Kowloon, Hong Kong SAR, China

†Equal contribution.

*Corresponding author.

Email: liang.an@polyu.edu.hk (L. An)

Abstract

Industrial production of ammonia remains dependent on energy-intensive Haber-Bosch process, causing huge environmental burdens. Electrochemical ammonia synthesis is a promising alternative approach capable of producing ammonia under the ambient condition via nitrogen reduction reaction on electrocatalysts. Although promising, this approach is still challenged by poor selectivity and low yield rate, requiring advanced electrocatalysts with rational designs for efficient nitrogen reduction reaction. Here we design and synthesize SnO_2 nanosheets with a unique two-dimensional layered architecture, potentially as an efficient electrocatalyst for ambient nitrogen reduction to ammonia. First, SnO_2 nanosheets with a thickness of few nanometers expose oriented crystalline (101) facets as a majority, preferably for nitrogen adsorption and reduction. Second, the presence of oxygen vacancies in SnO_2 nanosheets creates defective Sn nanostructures with dangling bonds, which can significantly enhance the nitrogen adsorption via strengthening the local binding effect between Sn and N atoms. Last, the two-dimensional architecture enables the presence of abundant uncoordinated surface atoms that are thermodynamically instable, in which nitrogen adsorption and dissociation mostly take place, thus greatly enhancing the catalytic reactivity. DFT

calculations found that the adsorption energy of N_2 molecules on (101) facet with two-coordinate oxygen vacancy is 10.45 kJ mol^{-1}, larger than that on (110) facet (4.60 kJ mol^{-1}). The strong binding between N_2 and abundantly exposed (101) facets facilitates the nitrogen adsorption and dissociation. Hence, two-dimensional layered SnO_2 is a promising electrocatalyst candidate for electrochemical ammonia synthesis. The ammonia production performance has been experimentally evaluated via construction of a three-electrode electrochemical cell, in which the as-prepared SnO_2 nanosheets grown on carbon cloth serves as working electrode, displaying an ammonia yield rate of 38.18 μg h^{-1} mg^{-1} and a Faradaic efficiency of 11.33%, both of which are higher than those achieved by most recently reported metal-based electrocatalysts. The ammonia production capability is also found stable, with a 93 % retention of ammonia yield rate after 6 cycles. Such a substantial improvement opens a window of opportunity for breakthroughs in the development of ambient ammonia synthesis technologies.

Keywords: Ambient ammonia synthesis; Nitrogen reduction reaction; SnO_2 nanosheets; Two-dimensional layered architecture; Rich exposed edges; Oxygen vacancies

1. Introduction

Ammonia is an important chemical in agriculture, pharmaceutical and textile industries,[1,2] which is industrially produced via a Haber-Bosch process[2] that converts atmospheric nitrogen to ammonia by a reaction with hydrogen using a metal catalyst under high temperatures and pressures. This significant achievement was awarded by three Nobel prizes in Chemistry in 1918, 1931 and 2007, respectively.[3] However, the Haber-Bosch process will annually consume more than 1 % global fossil fuels in order to create the reaction condition of high temperatures and pressures[4] and release carbon dioxide to the atmosphere. In response to energy and environmental consequences, therefore, much attention has been paid to developing green and sustainable ammonia synthesis technologies.[5–7]

Electrochemical ammonia synthesis is a promising alternative approach capable of producing ammonia under the ambient condition.[6] Since nitrogen is a stubbornly stable molecule, breaking it up typically requires an efficient electrocatalyst to achieve a high-performance electrochemical ammonia synthesis. Noble metal-based electrocatalysts have been proved to be efficient for nitrogen reduction reaction (NRR),[7] but their scarcity and high cost limit their massive applications in the ammonia industrial production. Alternatively, transitional metal-based electrocatalysts, such as Fe_2O_3 and MoS_2, become one of the promising candidates for efficient NRR because of their unique d-orbital structures.[8,9] The unoccupied d-orbital electrons have a major effect on the electron density of vicinal nitrogen molecules in terms of energy and configuration.[10,11] The transition metal will donate electrons to the π^* orbital of N≡N forming N-metal bond, thus weakening the N≡N triple bond and exhibiting a high reactivity toward nitrogen reduction. Nevertheless, the unoccupied d-orbital electrons also favor the formation of hydrogen-metal bond, reducing the activation energy of H-

H bond cleavage.[12] Hence, the two-electron-transfer hydrogen evolution reaction can be easily triggered, resulting in the competitive reactions between nitrogen reduction and hydrogen evolution, thus causing a poor selectivity issue.

Tin oxide (SnO_2), has been recently demonstrated to be a promising candidate as a highly selective electrocatalyst toward the NRR,[10,13] providing a new alternative beyond noble or transitional metal-based electrocatalysts. On one hand, SnO_2 is a semiconducting material offering a low flow rate of electrons during reduction reaction.[14] This feature dramatically suppresses the two-electron-transfer hydrogen evolution reaction, rather than the three-electron-transfer NRR, thus improving the selectivity toward ammonia production.[15] On the other hand, SnO_2 is a non-transitional metal oxide with very weak hydrogen adsorption, thus limiting the hydrogen evolution reaction.[10] However, previously reported SnO_2 nanoparticles[10,13] possess less exposed edges for nitrogen adsorption and random facets containing inactive catalytic surface for nitrogen reduction, thus showing an inferior NRR performance.

In this work, we design and synthesize two-dimensional (2D) layered SnO_2 nanosheets as an efficient electrocatalyst for ambient ammonia synthesis. First, 2D layered SnO_2 nanosheets, with a thickness of few nanometers, expose oriented and reactive (101) facets as a majority,[13] providing abundant active sites for nitrogen adsorption and dissociation. Second, the oxygen vacancies in SnO_2 nanosheets,[16] create defective nanostructures of Sn with dangling bonds, which further enhance the chemisorption of N_2 by strengthening binding effect between Sn and N. Last, the 2D architecture enables the appearance of uncoordinated surface atoms that are thermodynamically instable,[17] in which nitrogen adsorption and dissociation mostly take place, thereby substantially enhancing the NRR reactivity. DFT calculations further reveal a strong binding between N_2 and (101) facet with two-coordinate oxygen vacancy, facilitating the nitrogen

adsorption and dissociation, thus enhancing the NRR reactivity. The ammonia production performance is examined via construction of a three-electrode electrochemical cell, showing an ammonia yield rate of 38.18 $\mu g\, h^{-1}\, mg^{-1}$ and a Faradaic efficiency of 11.33 % at -0.25 V *vs.* RHE, both of which are much higher than those achieved by most recently reported metal-based electrocatalysts. The stability of ammonia production is also confirmed by cyclic test, preserving 93 % of the initial ammonia yield rate after 6 cycles.

2. Experimental section

2.1 Preparation and pretreatment of materials

SnO_2 nanosheets grown on carbon cloth (SnO_2@CC) as working electrode in a three-electrode electrochemical cell was prepared via a one-step hydrothermal process. A strip of carbon cloth (HESEN, Shanghai) was pre-treated in a concentrated HCl solution (38 %) for 2 h. Then, it was cleaned in deionized (DI) water and immersed into an autoclave containing 0.225 g $SnCl_2 \cdot 2H_2O$ and 0.9 g urea dissolved in 20 ml DI water. At last, it was hydrothermally treated in an oven at 200 ºC for 24 h for the growth of SnO_2 on carbon cloth. The mass loading of SnO_2 nanosheets is 0.8 mg cm^{-2}.

For the Nafion membrane, it was pre-treated differently for its usage in acid (pH = 3.5), neutral (pH = 7.0) and alkaline electrolytes (pH = 10.5). For acid and neutral electrolytes, it was separately boiled in 3.0 wt% H_2O_2 for 1 h and 1.0 M H_2SO_4 solution for 1 h, followed by DI water for 1 h. For alkaline electrolyte, it was boiled in 1.0 M KOH for 2 h and then washed with DI water.

2.2 Characterizations of materials

The structure of SnO_2@CC was characterized by X-ray diffraction (XRD) (D/max 2500PC), field emission scanning electron microscopy (FESEM) (Tescan MAIA3, Japan) and Raman spectra (Renishaw RM-1000, Britain) with 488 nm laser excitation.

The morphology of SnO_2@CC was examined by scanning transmission electron microscopy (TEM) using a Jeol JEM-2100F TEM microscope (Germany) and its crystal structure was revealed by selected area electron diffraction (SAED) pattern. The element analysis was conducted by energy-dispersive X-ray (EDX) and X-ray photoelectron spectroscopy (XPS), recorded by a spectrometer with Mg/Al Kα radiation (Thermo VG Scientific, USA). The electron paramagnetic resonance (EPR) spectra was measured at the X band 9.83 GHz using Bruker TMX spectrometer. The concentration of ammonia ions in test solution was detected by Ultraviolet (UV) adsorption spectra using UV-Vis double beam spectrophotometer (DB-20, Australia).

2.3 Electrochemical measurements

A three-electrode electrochemical cell was constructed to evaluate the ammonia production performance, in which SnO_2@CC was used as working electrode (1.0 × 3.0 cm^2), graphite paper (2.0 × 3.0 cm^2), purchased from Hebei thermal insulation engineering Co., Ltd, was used as counter electrode, and Hg/Hg_2SO_4 (MSE) was used as reference electrode in acid and neutral electrolytes, while Hg/HgO (MOE) was used as reference electrode in alkaline electrolyte. The potentials were converted to reversible hydrogen electrode (RHE) by the following equations[18]:

$$E_{RHE} = E_{SCE} + 0.059\text{pH} + 0.616 \text{ (MSE)} \quad (1)$$

$$E_{RHE} = E_{SCE} + 0.059\text{pH} + 0.098 \text{ (MOE)} \quad (2)$$

0.5 M K_2SO_4 dissolved in 200 mL DI water served as the electrolyte. Nafion 115 membrane was employed to separate two compartments and transport protons. Two bottles of dilute sulfuric acid (0.05 M) were used to remove the ammonia impurity from the nitrogen source. A liquid seal was used at the end of gas outlet to avoid the gas impurities. Before the examination of ammonia production performance, nitrogen was consistently inputted into the anodic compartment of three-electrode electrochemical

cell with a flow rate of 20 ml/min for 1 h to obtain N_2-saturated electrolyte. During cell operation, the electrolyte was constantly stirring with a stirring rate of 200 r/s to make dissolved nitrogen well dispersed. The working electrode previously used was carefully washed with DI water for 8 times and then dried, being ready for next-cycle test of ammonia production performance. All the electrochemical measurements were performed using Multi-Autolab electrochemical workstation (M204, Switzerland).

2.4 Determination of ammonia and hydrazine

The indophenol blue method is used to determine the ammonia concentration in the test solution. For the preparation of chromogenic solution, 1.0 mL mixed solution was prepared by adding 1.0 M NaOH, sodium citrate (3.0 wt. %) and salicylic acid (3.0 wt. %), 0.5 mL sodium hypochlorite solution (5.0 wt. %) and 0.1 mL sodium nitroferricyanide dihydrate (1.0 wt. %). Additional 1.0 mL test solution was added to the mixed solution and stayed for 2 h before UV-Vis adsorption test. For the preparation of standard solution with a certain amount of ammonia ions, NH_4Cl was added into the DI water to prepare solutions with different ammonia-ion concentrations (0.03125, 0.0625, 0.125, 0.25, 0.5 and 1.0 mg/L). Then, H_2SO_4 or KOH was added into solutions to tailor the pH value of solution to 3.5, 7.0 or 10.5. The same strategy was employed for the preparation of electrolyte with different pH values.

The possible production of hydrazine was identified by the method of Watt and Chrisp.[19] First, a mixed solution of 0.599 g $C_9H_{11}NO$, 3.0 ml concentrated HCl (38 %) and 30 ml ethanol was prepared and used as the color reagent. Second, a series of N_2H_4 solutions with known concentrations (0.3125, 0.625, 1.25, 2.5, 5.0 mg/L) are prepared and used as standard solutions. Third, 1.0 ml color reagent and 1.0 ml standard solutions were mixed with each other and stirred for 20 min. Last, the obtained mixed solution was transferred to UV-Vis double beam spectrophotometer and tested, by measuring

the absorbance at 457 nm. As a result, a linear relationship between absorbance and concentration of hydrazine hydrate is constructed, showing a good linear fit (y = 0.16154 + 0.36556 x, R^2 = 0.999). For the determination of possible production of hydrazine, 1.0 ml solution was taken out after 2-hour cell operation in N_2 and mixed with 1.0 ml color reagent. The subsequent color rendering and measurements follow the same procedures as the standard N_2H_4 solutions.

2.5 First-principles calculations

DFT calculations were performed using the Vienna Ab-initio Simulation Package (VASP) code.[20,21] For the total energy calculations, the plane wave cutoff energy was 400 eV. Ion–electron interactions were represented by ultrasoft pseudopotentials within the framework of the projector-augmented wave (PAW) method.[22] The generalized gradient approximation (GGA) with the Perdew–Burke–Ernzerhof (PBE) functional was adopted as the exchange-correlation functional.[23] The Brillouin zone integration was approximated by a sum over special selected k-points using the 2×2×1 MonkhorstPack method.[24] The geometries were optimized until the energy was converged to 1×10^{-5} eV/atom and the forces to 0.02 eV/Å.

For SnO_2(101) and SnO_2(110), during the calculations, the bottom one layer is fixed, other layers and the adsorbed species are relaxed; moreover, in order to eliminate the interactions between slabs, the vacuum region is set to 15 Å in the z direction to separate the slabs. The adsorption energy of gas molecules is given by the equation:

$$E_{ads} = E_{tot} - Es - E_m \quad (3)$$

where E_{tot} is the ground state energy of the surface with the adsorbed molecule, E_s is the initial energy of the surface slab, and E_m is that for the molecule.

3. Results and discussion

SnO_2 nanosheets are densely grown on carbon cloth (Figure 1a), owning an ultrathin layered structure with very sharp edges, as evidenced by the enlarged picture in Figure 1b. Abundant void space between SnO_2 nanosheets, with a size of tens of nanometers, facilitates the infiltration of electrolyte, exposing the basal planes of SnO_2 to the electrolyte and thus providing sufficient solid-electrolyte interfaces. Figure 1c gives a side view of 2D SnO_2 nanosheets, observing the basal planes of SnO_2 with sharp edges protruding outwards. To enrich topographical information of SnO_2 nanosheets, we have further examined the SnO_2 nanosheets by SEM from x, y and z axis directions, as shown in Figure S1. The interface between SnO_2 nanosheets and carbon substrate can be clearly observed (Figure S1b), and the lateral size of SnO_2 nanosheets is in the range of tens of nanometers to hundreds of nanometers (Figure S1d). Ultrathin SnO_2 nanosheets observed by TEM are in good agreement with SEM images, with the observation of dark and oriental stripes (Figure 1d). We further reveal the edge structures and basal planes of SnO_2 nanosheets by HRTEM images, as shown in Figure 1e-f. The sharp edge perpendicular to the carbon surface, containing 20 layers of SnO_2 with an interlayer spacing of 0.264 nm, as evidenced in Figure 1h, corresponding to (101) facets of SnO_2. The exposure of (101) facets is due to the preferential growth of SnO_2 nanosheets along the (101) direction.[13] The basal plane of SnO_2 nanosheets owns an interlayer spacing of 0.334 nm (Figure 1i), which corresponds to (110) facets of SnO_2. The crystal structure of SnO_2 are revealed by SAED pattern (Figure 1g), showing discrete spots indexed to the (101), (110), and (211) facets of SnO_2,[25] and the blurred aperture in the pattern derives from the carbon substrate with poor crystallization. Notably, the diffraction spots of (101) facet is most obvious, which is in good agreement with abundant exposed (101) facets of 2D layered SnO_2 nanosheets. The elements in the sample, examined by EDX spectrum (Figure S2), contains Sn, C, O and Cu signals, in which Cu signal comes

from the mesh carrier, without observing impurities in the sample.

A cassiterite phase of SnO_2 was demonstrated by XRD pattern,[26] displaying three characteristic diffraction peaks at 26.61º, 33.89º and 51.78º, indexed to the (110), (101) and (211) planes of SnO_2 (JCPDS No. 41-1445), in good agreement with the observation of three pairs of diffraction spots in SAED pattern (Figure 1g). Broad peaks at around 26º and 43º are characteristic peaks of non-graphitizable carbon, indicating the poor crystallization of carbon cloth. No other impurities are found in the sample, observing only peaks of Sn, O and C at different atomic orbitals in XPS spectra (Figure 2b). The tetravalent tin (Sn^{4+}) in the sample is confirmed by observing a binding energy gap of 8.4 eV between two separated peaks of $Sn3d_{5/2}$ (487.38 eV) and $Sn3d_{3/2}$ (495.78 eV), which are deconvoluted from the high-resolution 3d peaks.[27] The O1s spectra can be fitted into three deconvoluted peaks, including Sn^{4+}-O at 530.2 ± 0.3 eV, Sn-O-C at 531.6 ± 0.3 eV[27] and the loss of oxygen at 532.6 ± 0.3 eV, which is an indicator of oxygen vacancies.[28] Oxygen vacancies in SnO_2 nanosheets are further confirmed by EPR spectra (Figure S3).[29] The EPR spectra of SnO_2 nanosheets displays a distinct ferromagnetic behavior with a EPR signal at g = 1.89, which is assigned to an unpaired electron produced by the defect reaction $V_O^{\times} \rightarrow V_O^{\cdot} + e'$, in which $V_O^{\times}$ represents the neutral oxygen vacancies and $V_O^{\cdot}$ represents the singly ionized oxygen vacancies ($V_O^{\cdot}$ in Kroger-Vink notation).[29] The generation of neutral oxygen vacancies is due to the reactions between the surface oxygen atoms in SnO_2 and ammonia via the following reaction[30,31]:

$$SnO_2 + NH_3 \rightarrow 1/2N_2 + SnO_{2-x} + 3/2H_2O \quad (4)$$

Where ammonia is produced by the decomposition of urea during hydrothermal reaction. Such feature gives rise to defective Sn nanostructures, facilitating the adsorption of N_2 by strengthening Sn-N bonding, thus enhancing NRR reactivity.[32]

Electrochemical measurements were carried out via construction of a three-electrode electrochemical cell, as shown in Figure S5. The voltage window for nitrogen reduction is initially determined by referring to the Pourbaix diagram of Sn (Figure S6), in which SnO_2 phase is found to be stable in acidic electrolyte even though a negative potential is applied, thus showing promises for ammonia synthesis in acidic electrolyte system. Theoretically, SnO_2 will be reduced to soluble $SnOH^+$ when applying a negative potential of -0.2 V in acidic electrolyte (pH = 3.5), as evidenced in Figure S6b. In practical applications, however, a more negative potential than -0.2 V is generally required. The voltage window for nitrogen reduction is experimentally examined by linear sweep voltammetry (LSV) tests under different conditions of fed gases (Ar or N_2). Pristine carbon cloth is first investigated in acidic electrolyte (pH = 3.5), displaying flat curves with a current response close to 0 mA cm^{-2} (Figure 3a), which indicates the inert nature of carbon cloth when a negative potential is applied. In contrast, current slopes are observed when studying the SnO_2@CC electrode, which may derive from multiple electrochemical reactions including hydrogen evolution.[33–35] Notably, the difference in current under different gas conditions is observed in the voltage range from -0.186 V to -0.4 V (*vs.* RHE), which can only be attributed to the NRR by considering the inert nature of Ar gas. Similarly, the difference in current is also observed in neutral (pH = 7.0) and alkaline electrolyte (pH = 10.5), indicating that the NRR can be achieved in different electrolyte systems. Notably, the onset potential of the NRR is positively shifted as the pH value of electrolyte increases, which limits the hydrogen evolution and preferably reduce nitrogen to ammonia. Hence, the acidic electrolyte is the most appropriate media to achieve ammonia production with high selectivity.

The feasibility of ammonia production is examined by detecting the UV-Vis absorbance of test solutions after cell operation, and the amount of ammonia production can be quantified by comparing with the standard UV adsorption curves, as shown in Figure S7. Relationships between the concentration of ammonia ions and adsorption peak intensities are constructed, with a good linear fit ($R^2 > 0.999$) in different electrolyte systems. For the catalytic performance of SnO_2@CC electrode at -0.2 V under the N_2 condition, successful ammonia synthesis can be confirmed by observing a distinct UV adsorption peak centered at around 652 nm (Figure S8). In comparison, for the catalytic performance of SnO_2@CC electrode in Ar-saturated electrolyte, basically no UV adsorption peak can be observed before and after cell operation (Figure S8 and Figure S9), revealing that the ammonia production only results from the reduction of fed N_2. Under open-circuit condition (Figure S8), almost no ammonia can be detected after 2-h cell operation, showing the NRR cannot be triggered without applying negative potentials and eliminating the possibility of ammonia contamination during ammonia production. In addition, almost no ammonia can be detected when using carbon cloth as working electrode (Figure S8), thus precluding the contribution of ammonia production from carbon cloth.

From the I-t curves depicted in Figure 4a and Figure S10, the current densities in N_2 are larger than those in Ar at applied potentials ranging from -0.10 V to -0.35 V (vs. *RHE*), demonstrating the NRR reactivity of SnO_2 nanosheets. In addition, the current densities in N_2 remain steady during 2-h operation at different potentials from -0.10 V to -0.35 V, suggesting the stable ammonia production performance. However, the current density is dramatically enlarged at -0.40 V and gradually decayed during operation, which may be attributed to the reduction of SnO_2. The amount of ammonia

production after 2-h operation is quantitively determined, and ammonia yield rates at different potentials are calculated by the following equation[36]:

$$r_{NH3} = (n \times V)/(t \times A) \quad (3)$$

where n represents the ammonia concentration, V stands for the volume of the electrolyte, t is the reaction time, and A is the geometric area of electrodes immersed in the electrolyte. A maximum ammonia yield rate of 38.18 $\mu g\, h^{-1}\, mg^{-1}$ is observed at -0.25 V (Figure 4c), and it gradually decreases as the potential becomes more negative due to the more intense hydrogen evolution. The Faradaic efficiencies are calculated by the following equation[36]:

$$FE\ \ (\%) = (3F \times n \times V)/(M \times Q) \quad (4)$$

where F represents the Faraday constant, n is the measured NH_3 concentration, V stands for the volume of the electrolyte, M is the relative molecular mass of N, NH_3, or NH_4^+ (taking standard curve as criterion), and Q represents the total charge used during cell operation. A high Faradaic efficiency of 11.33 % is observed at -0.25 V, showing 2D layered SnO_2 nanosheets own excellent selectivity toward the NRR. The ammonia production performance in acidic electrolyte are much more superior than other electrolyte systems (Figure S11), in good agreement with the previous observation on onset potentials (Figure 3). Moreover, both yield rates and Faradaic efficiencies are much higher than the most reported metal-based electrocatalysts,[10,13,44–47,32,37–43] as shown in Figure S12 and Table S1. The stability of ammonia production is also evaluated by cyclic test (Figure 4d), showing a 93 % retention of ammonia yield rate and preserving a Faradaic efficiency of 10.3 % after 6 cycles, demonstrating the capability of SnO_2@CC electrode for continuous ammonia production. The crystal structures and surface morphologies of SnO_2@CC electrode remains basically

unchanged after 6-h cell operation at -0.35 V, revealed by XRD pattern (Figure S13a) and SEM image (Figure S13c). However, the crystal structures of SnO_2@CC electrode change after 6-h cell operation at -0.40 V, observing decreased characteristic peaks of SnO_2. Together with the distinct pattern collapse of SnO_2@CC electrode (Figure S13d) forming clusters, it can be concluded that SnO_2 will be partially reduced into soluble $SnOH^+$ at -0.40 V but remains stable above -0.35 V during ammonia production.

The yield rate of N_2H_4 in N_2 was also examined by the Watt and Chrisp method,[5] in which a series of N_2H_4 solutions with known concentrations are used to measure their UV-vis absorbance and to plot a calibration curve (Figure S14). Resultantly, no peaks appear at 457 nm at applied potentials from -0.2 V to -0.4 V (vs. RHE), as shown in Figure S15. Hence, no N_2H_4 was detected during cell operation in N_2.

DFT calculations are conducted to study the NRR reactivity on SnO_2 facets with oxygen vacancies. The (101) and (110) facets are the two main exposed facets of SnO_2 nanosheets, as evidenced by TEM images (Figures 2h-i). There are two types of oxygen on these facets. One is the two-coordinate bridging O, and the other is the three-coordinate in-plane O, as shown in Figure S16. In order to study N_2 adsorption on these facets with oxygen vacancies, the foremost task is to find out the most stable form of oxygen vacancies on these facets, since steady-state NRR reactivity highly depends on oxygen vacancies with structural stability. Here, the total energy of crystal facets with different oxygen vacancies is studied by DFT calculation, as shown in the Table S2. During structural optimization, we found that if a three-coordinate oxygen atom on the (101) facet is removed, a two-coordinated oxygen on the surface will fill into this vacant position, forming a two-coordinate oxygen vacancy. Therefore, only the two-coordinate oxygen vacancies on (101) facets are stable. As for oxygen vacancies on (110) facets, two-coordinate oxygen vacancies are more stable than three-coordinate oxygen

vacancies. Then, we investigate the N_2 adsorption on (101) and (110) facets with a two-coordinate oxygen vacancy. The adsorption of N_2 molecules on (101) facet shows an adsorption energy of 10.45 kJ mol^{-1}, which is larger than that on (110) facet with an adsorption energy of 4.60 kJ mol^{-1}. Hence, the strong binding between N_2 and abundantly exposed (101) facet facilitates the NRR.

4. **Concluding remarks**

In this work, we achieve ambient ammonia synthesis via using efficient and cost-effective 2D layered SnO_2 nanosheets, providing an alternative to Haber-Bosch process. The abundant and exposed (101) facets, the presence of oxygen vacancies in SnO_2, together with uncoordinated surface atoms enabled by its unique 2D architecture, are favorable for nitrogen adsorption and reduction, thus exhibiting superior NRR reactivity and selectivity. DFT calculations reveal a strong binding between N_2 molecules and (101) facets with two-coordinate oxygen vacancies, facilitating the nitrogen adsorption and dissociation. As a result, the constructed electrochemical cell using SnO_2@CC as working electrode exhibits an ammonia yield rate of 38.18 $\mu g\, h^{-1}\, mg^{-1}$ and a Faradaic efficiency of 11.33% at -0.25 V, much higher than the most recently reported metal-based electrocatalysts. This work not only provides us an attractive electrocatalyst material for the NRR in acidic media, but also opens up an exciting new window of opportunity to the rational design and fabrication of non-transitional metal oxides for efficient ammonia synthesis.

Supporting Information:

SEM images, TEM images, EDX element analysis, EPR spectra of SnO_2 nanosheets; Cell configuration; Pourbaix diagram of Sn; Calibration plots of ammonia and hydrazine; Control experiments for the confirmation of NRR reactivity; Ammonia

production performance in neutral and alkaline electrolyte; Performance comparison with the open literatures; O configurations in SnO_2 and energy calculations of crystal facets with oxygen vacancies.

Conflicts of interest:

There are no conflicts to declare.

Acknowledgement:

This work was fully supported by a grant from the Research Grants Council of the Hong Kong Special Administrative Region, China (Project No. 15222018).

References

(1) Medford, A. J.; Hatzell, M. C. Photon-Driven Nitrogen Fixation: Current Progress, Thermodynamic Considerations, and Future Outlook. *ACS Catal.* **2017**, *7*, 2624–2643.

(2) Zhao, Y.; Shi, R.; Bian, X.; Zhou, C.; Zhao, Y.; Zhang, S.; Wu, F.; Waterhouse, G. I. N.; Wu, L. Z.; Tung, C. H.; Zhang, T. Ammonia Detection Methods in Photocatalytic and Electrocatalytic Experiments: How to Improve the Reliability of NH 3 Production Rates? *Adv. Sci.* **2019**, *6*, 1802109.

(3) Foster, S. L.; Bakovic, S. I. P.; Duda, R. D.; Maheshwari, S.; Milton, R. D.; Minteer, S. D.; Janik, M. J.; Renner, J. N.; Greenlee, L. F. Catalysts for Nitrogen Reduction to Ammonia. *Nat. Catal.* **2018**, *1*, 490–500.

(4) Guo, X.; Du, H.; Qu, F.; Li, J. Recent Progress in Electrocatalytic Nitrogen Reduction. *J. Mater. Chem. A* **2019**, *7*, 3531–3543.

(5) Kim, K.; Lee, N.; Yoo, C. Y.; Kim, J. N.; Yoon, H. C.; Han, J.-I. Communication-Electrochemical Reduction of Nitrogen to Ammonia in 2-Propanol under Ambient Temperature and Pressure. *J. Electrochem. Soc.* **2016**, *163*, F610–F612.

(6) Légaré, M. A.; Bélanger-Chabot, G.; Dewhurst, R. D.; Welz, E.; Krummenacher, I.; Engels, B.; Braunschweig, H. Nitrogen Fixation and Reduction at Boron. *Science.* **2018**, *359*, 896–900.

(7) Suryanto, B. H. R.; Du, H. L.; Wang, D.; Chen, J.; Simonov, A. N.; MacFarlane, D. R. Challenges and Prospects in the Catalysis of Electroreduction of Nitrogen to Ammonia. *Nat. Catal.* **2019**, *2*, 290–296.

(8) Jin, H.; Li, L.; Liu, X.; Tang, C.; Xu, W.; Chen, S.; Song, L.; Zheng, Y.; Qiao, S. Z. Nitrogen Vacancies on 2D Layered W_2N_3: A Stable and Efficient Active Site for Nitrogen Reduction Reaction. *Adv. Mater.* **2019**, *31*, 1–8.

(9) Guo, C.; Ran, J.; Vasileff, A.; Qiao, S. Z. Rational Design of Electrocatalysts and Photo(Electro)Catalysts for Nitrogen Reduction to Ammonia (NH 3) under Ambient Conditions. *Energy Environ. Sci.* **2018**, *11*, 45–56.

(10) Chu, K.; Liu, Y. P.; Li, Y. B.; Wang, J.; Zhang, H. Electronically Coupled SnO2 Quantum Dots and Graphene for Efficient Nitrogen Reduction Reaction. *ACS Appl. Mater. Interfaces* **2019**, *11*, 31806–31815.

(11) Zhang, L.; Ding, L.; Chen, G. F.; Yang, X.; Wang, H.; Ding, L. X. X.; Wang, H.; Zhang, L. Ammonia Synthesis Under Ambient Conditions: Selective Electroreduction of Dinitrogen to Ammonia on Black Phosphorus Nanosheets. *Angew. Chemie - Int. Ed.* **2019**, *58*, 2612–2616.

(12) Li, M.; Huang, H.; Low, J.; Gao, C.; Long, R.; Xiong, Y. Recent Progress on Electrocatalyst and Photocatalyst Design for Nitrogen Reduction. *Small Methods* **2019**, *3*, 1800388.

(13) Zhang, L.; Ren, X.; Luo, Y.; Shi, X.; Asiri, A. M.; Li, T.; Sun, X. Ambient NH3 Synthesis via Electrochemical Reduction of N2 over Cubic Sub-Micron SnO2 Particles. *Chem. Commun.* **2018**, *54*, 12966–12969.

(14) Van Der Ham, C. J. M.; Koper, M. T. M.; Hetterscheid, D. G. H. Challenges in Reduction of Dinitrogen by Proton and Electron Transfer. *Chem. Soc. Rev.* **2014**, *43*, 5183–5191.

(15) Li, L.; Tang, C.; Xia, B.; Jin, H.; Zheng, Y.; Qiao, S. Z. Two-Dimensional Mosaic Bismuth Nanosheets for Highly Selective Ambient Electrocatalytic Nitrogen Reduction. *ACS Catal.* **2019**, *9*, 2902–2908.

(16) Wang, C.; Du, G.; Ståhl, K.; Huang, H.; Zhong, Y.; Jiang, J. Z. Ultrathin SnO 2 Nanosheets: Oriented Attachment Mechanism, Nonstoichiometric Defects, and Enhanced Lithium-Ion Battery Performances. *J. Phys. Chem. C* **2012**, *116*, 4000–4011.

(17) Hu, S.; Qiao, P.; Zhang, L.; Jiang, B.; Gao, Y.; Hou, F.; Wu, B.; Li, Q.; Jiang, Y.; Tian, C.; Zhou, W.; Tian, G. H.; Fu, H. G. Assembly of TiO_2 Ultrathin Nanosheets with Surface Lattice Distortion for Solar-Light-Driven Photocatalytic Hydrogen Evolution. *Appl. Catal. B Environ.* **2018**, *239*, 317–323.

(18) Liu, Y.; Li, D.; Yu, J.; Ding, B. Stable Confinement of Black Phosphorus Quantum Dots on Black Tin Oxide Nanotubes: A Robust, Double-Active Electrocatalyst toward Efficient Nitrogen Fixation. *Angew. Chemie* **2019**, *131*, 16591–16596.

(19) Watt, G. W.; Chrisp, J. D. Spectrophotometric Method for Determination of Hydrazine. *Anal. Chem.* **1952**, *24*, 2006–2008.

(20) Kresse, G.; Furthmüller, J. Efficient Iterative Schemes for Ab Initio Total-Energy Calculations Using a Plane-Wave Basis Set. *Phys. Rev. B* **1996**, *54*, 11169–11186.

(21) Kresse, G.; Furthmüller, J. Efficiency of Ab-Initio Total Energy Calculations for Metals and Semiconductors Using a Plane-Wave Basis Set. *Comput. Mater. Sci.* **1996**, *6*, 15–50.

(22) Blöchl, P. E. Projector Augmented-Wave Method. *Phys. Rev. B* **1994**, *50*, 17953–17979.

(23) Perdew, J. P.; Burke, K.; Ernzerhof, M. Generalized Gradient Approximation Made Simple. *Phys. Rev. Lett.* **1996**, *77*, 3865–3868.

(24) Pack, J. D.; Monkhorst, H. J. Special Points for Brillouin-Zone Integrations. *Phys. Rev. B* **1977**, *16*, 1748–1749.

(25) Zhang, Y.; Hu, Z.; Liang, Y.; Yang, Y.; An, N.; Li, Z.; Wu, H. Growth of 3D SnO2 Nanosheets on Carbon Cloth as a Binder-Free Electrode for Supercapacitors. *J. Mater. Chem. A* **2015**, *3*, 15057–15067.

(26) Zhang, L.; Ge, S.; Zuo, Y.; Zhang, B.; Xi, L. Influence of Oxygen Flow Rate on the Morphology and Magnetism of SnO 2 Nanostructures. *J. Phys. Chem. C* **2010**, *114*, 7541–7547.

(27) Wang, Y. Y.; Hou, B. H.; Wang, Y. N.; Lü, H. Y.; Guo, J. Z.; Ning, Q. L.; Zhang, J. P.; Lü, C. L.; Wu, X. L. Multiple Heterointerfaces Boosted De-/Sodiation Kinetics towards Superior Na Storage and Na-Ion Full Battery. *J. Mater. Chem. A* **2018**, *6*, 6578–6586.

(28) Daiyan, R.; Lu, X.; Saputera, W. H.; Ng, Y. H.; Amal, R. Highly Selective Reduction of CO2 to Formate at Low Overpotentials Achieved by a Mesoporous Tin Oxide Electrocatalyst. *ACS Sustain. Chem. Eng.* **2018**, *6*, 1670–1679.

(29) Godinho, K. G.; Walsh, A.; Watson, G. W. Energetic and Electronic Structure Analysis of Intrinsic Defects in SnO_2. *J. Phys. Chem. C* **2009**, *113*, 439–448.

(30) Shao, F.; Hoffmann, M. W. G.; Prades, J. D.; Morante, J. R.; López, N.; Hernández-Ramírez, F. Interaction Mechanisms of Ammonia and Tin Oxide: A Combined Analysis Using Single Nanowire Devices and DFT Calculations. *J. Phys. Chem. C* **2013**, *117*, 3520–3526.

(31) Shao, F.; Hernandez-Ramirez, F.; Prades, J. D.; Morante, J. R.; Lopez, N. Assessment and Modeling of NH_3-SnO_2 Interactions Using Individual Nanowires. *Procedia Engineering* **2012**, *47*, 293 – 297.

(32) Wu, T.; Zhu, X.; Xing, Z.; Mou, S.; Li, C.; Qiao, Y.; Liu, Q.; Luo, Y.; Shi, X.; Zhang, Y.; Sun, X. Greatly Improving Electrochemical N_2 Reduction over TiO_2 Nanoparticles by Iron Doping. *Angew. Chemie - Int. Ed.* **2019**, *58*, 18449–18453.

(33) Huang, Y.; Miao, Y. E.; Fu, J.; Mo, S.; Wei, C.; Liu, T. Perpendicularly Oriented Few-Layer $MoSe_2$ on SnO_2 Nanotubes for Efficient Hydrogen Evolution Reaction. *J. Mater. Chem. A* **2015**, *3*, 16263–16271.

(34) Huang, Y.; Miao, Y. E.; Zhang, L.; Tjiu, W. W.; Pan, J.; Liu, T. Synthesis of Few-Layered MoS2 Nanosheet-Coated Electrospun SnO2 Nanotube Heterostructures for Enhanced Hydrogen Evolution Reaction. *Nanoscale* **2014**, *6*, 10673–10679.

(35) Ravula, S.; Zhang, C.; Essner, J. B.; Robertson, J. D.; Lin, J.; Baker, G. A. Ionic Liquid-Assisted Synthesis of Nanoscale $(MoS_2)_x(SnO_2)_{1-x}$ on Reduced Graphene Oxide for the Electrocatalytic Hydrogen Evolution Reaction. *ACS Appl. Mater. Interfaces* **2017**, *9*, 8065–8074.

(36) Chen, G.-F.; Ren, S.; Zhang, L.; Cheng, H.; Luo, Y.; Zhu, K.; Ding, L.-X.; Wang, H. Advances in Electrocatalytic N_2 Reduction-Strategies to Tackle the Selectivity Challenge . *Small Methods* **2019**, *3*, 1800337.

(37) Shi, M. M.; Bao, D.; Wulan, B. R.; Li, Y. H.; Zhang, Y. F.; Yan, J. M.; Jiang, Q. Au Sub-Nanoclusters on TiO_2 toward Highly Efficient and Selective Electrocatalyst for N_2 Conversion to NH_3 at Ambient Conditions. *Adv. Mater.* **2017**, *29*, 2–7.

(38) Bao, D.; Zhang, Q.; Meng, F. L.; Zhong, H. X.; Shi, M. M.; Zhang, Y.; Yan, J. M.; Jiang, Q.; Zhang, X. B. Electrochemical Reduction of N_2 under Ambient Conditions for Artificial N_2 Fixation and Renewable Energy Storage Using N_2 /NH_3 Cycle. *Adv. Mater.* **2017**, *29*, 1604799.

(39) Hu, L.; Khaniya, A.; Wang, J.; Chen, G.; Kaden, W. E.; Feng, X. Ambient Electrochemical Ammonia Synthesis with High Selectivity on Fe/Fe Oxide Catalyst. *ACS Catal.* **2018**, *8*, 9312–9319.

(40) Han, Z.; Choi, C.; Hong, S.; Wu, T. S.; Soo, Y. L.; Jung, Y.; Qiu, J.; Sun, Z. Activated TiO_2 with Tuned Vacancy for Efficient Electrochemical Nitrogen Reduction. *Appl. Catal. B Environ.* **2019**, *257*, 117896.

(41) Zhao, X.; Zhang, X.; Xue, Z.; Chen, W.; Zhou, Z.; Mu, T. Fe Nanodot-Decorated MoS2 Nanosheets on Carbon Cloth: An Efficient and Flexible Electrode for Ambient Ammonia Synthesis. *J. Mater. Chem. A* **2019**, *7*, 27417–27422.

(42) Xie, H.; Geng, Q.; Zhu, X.; Luo, Y.; Chang, L.; Niu, X.; Shi, X.; Asiri, A. M.; Gao, S.; Wang, Z.; Sun, X. PdP_2 Nanoparticles-Reduced Graphene Oxide for Electrocatalytic N_2 Conversion to NH_3 under Ambient Conditions. *J. Mater. Chem. A* **2019**, *7*, 24760–24764.

(43) Huang, H.; Li, F.; Xue, Q.; Zhang, Y.; Yin, S.; Chen, Y. Salt-Templated Construction of Ultrathin Cobalt Doped Iron Thiophosphite Nanosheets toward Electrochemical Ammonia Synthesis. *Small* **2019**, *15*, 1–11.

(44) Lai, F.; Feng, J.; Ye, X.; Zong, W.; He, G.; Yang, C.; Wang, W.; Miao, Y. E.; Pan, B.; Yan, W.; Liu, T.; Parkin, I. P. Oxygen Vacancy Engineering in Spinel-Structured Nanosheet Wrapped Hollow Polyhedra for Electrochemical Nitrogen Fixation under Ambient Conditions. *J. Mater. Chem. A* **2020**, *8*, 1652–1659.

(45) Chang, B.; Deng, L.; Wang, S.; Shi, D.; Ai, Z.; Jiang, H.; Shao, Y.; Zhang, L.; Shen, J.; Wu, Y.; Hao, X. A Vanadium-Nickel Oxynitride Layer for Enhanced Electrocatalytic Nitrogen Fixation in Neutral Media. *J. Mater. Chem. A* **2019**, *8*, 91–96.

(46) Liu, J.; Kong, X.; Zheng, L.; Guo, X.; Liu, X.; Shui, J. Rare Earth Single-Atom Catalysts for Nitrogen and Carbon Dioxide Reduction. *ACS Nano* **2020**, *14*, 1093–1101.

(47) Wei, P.; Xie, H.; Zhu, X.; Zhao, R.; Ji, L.; Tong, X.; Luo, Y.; Cui, G.; Wang, Z.; Sun, X. CoS_2 Nanoparticles-Embedded N-Doped Carbon Nanobox Derived from ZIF-67 for Electrocatalytic N_2-to-NH_3 Fixation under Ambient Conditions. *ACS Sustain. Chem. Eng.* **2020**, *8*, 29–33.

Figures:

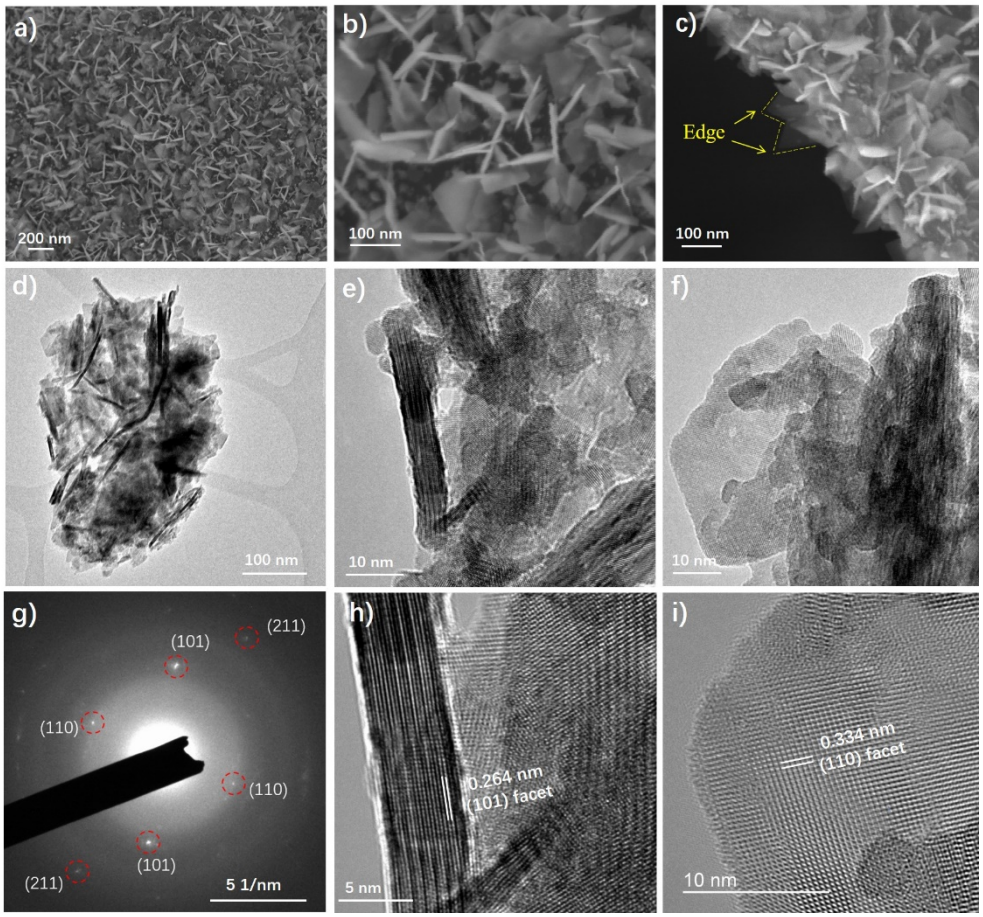

Figure 1 (a) Surface morphology of SnO_2@carbon cloth and (b) 2D layered SnO_2 nanosheets with sharp and exposed edges revealed by SEM images. (c) A side view of SnO_2 nanosheets with sharp edges. (d-f) The observation of edges and planes of SnO_2 nanosheets by TEM images. Figure 1e and Figure 1f are enlarged pictures of Figure 1d. (g) Observation of diffraction spots of (101), (110) and (211) facets in SAED pattern. (h) An enlarged picture of Figure 1e, showing an edge of SnO_2 nanosheets with an interlayer spacing of 0.264 nm, corresponding to (101) facet. (i) An enlarged picture of Figure 1f, showing a basal plane of SnO_2 nanosheets with an interlayer spacing of 0.334 nm, corresponding to (110) facet.

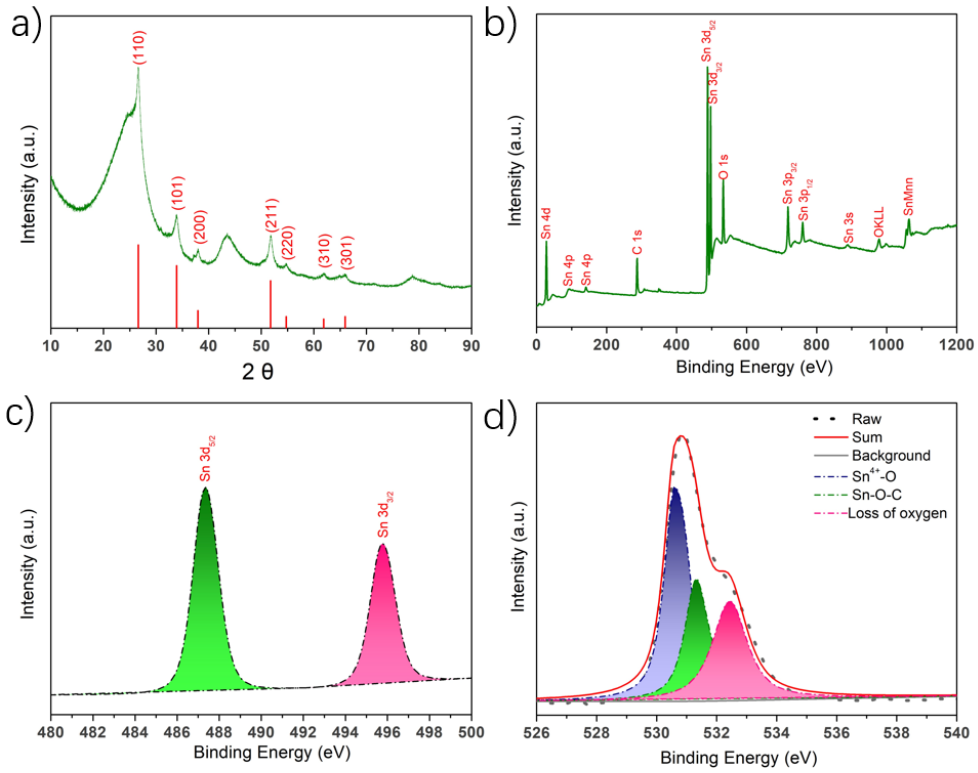

Figure 2 Phase and composition analysis of SnO_2@CC. (a) XRD pattern of the sample comparing with standard pattern of SnO_2 (JCPDS No. 41-1445). (b) XPS full spectrum of SnO_2@CC showing the presence of three elements of Sn, O and C. (c) The partial scan of Sn 3d spectrum showing the existence of Sn^{4+} in the final product. (d) Deconvoluted O1s spectra showing the presence of oxygen vacancies.

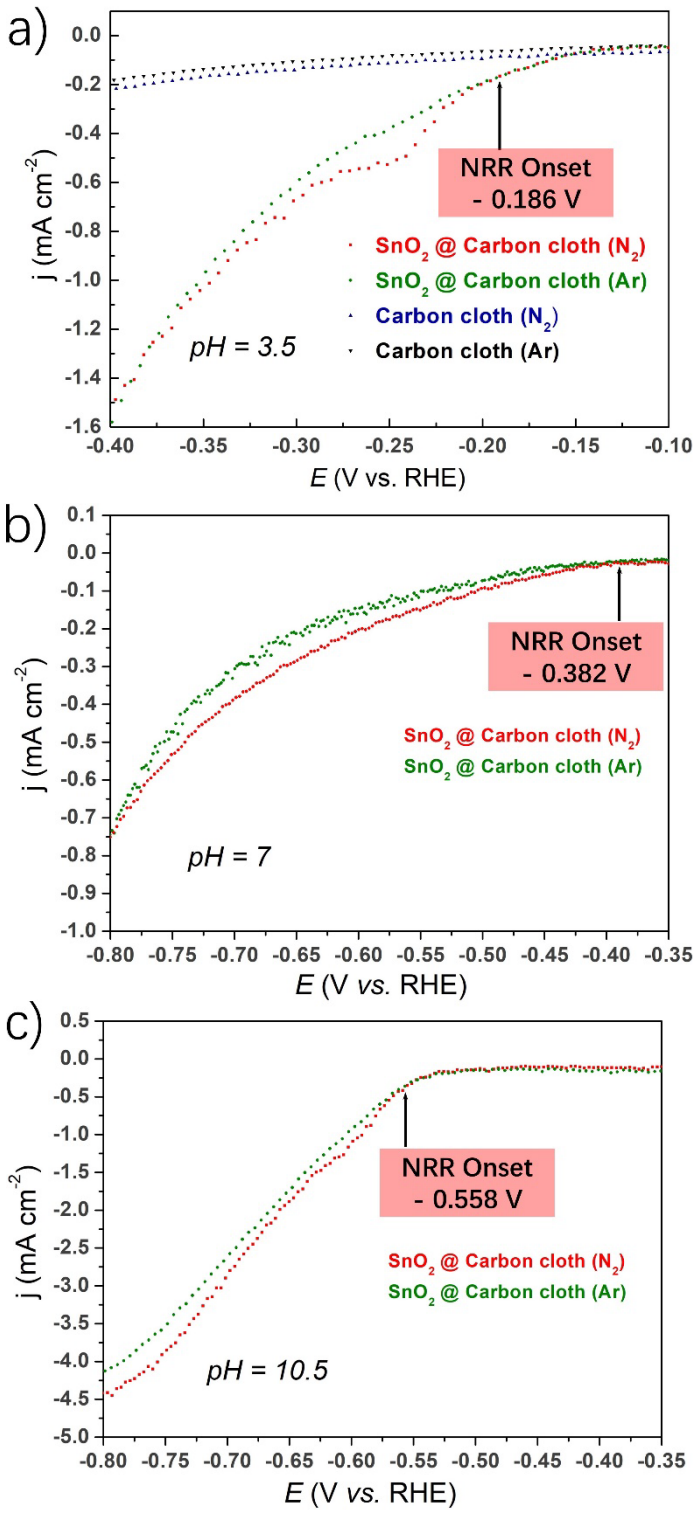

Figure 3 LSV tests under different conditions for revealing the appropriate voltage window of NRR. In the cathodic scan, the abscissa corresponding to the starting point of curve branch represents the onset potential for NRR. (a) pH = 3.5. (b) pH = 7.0. (c) pH = 10.5.

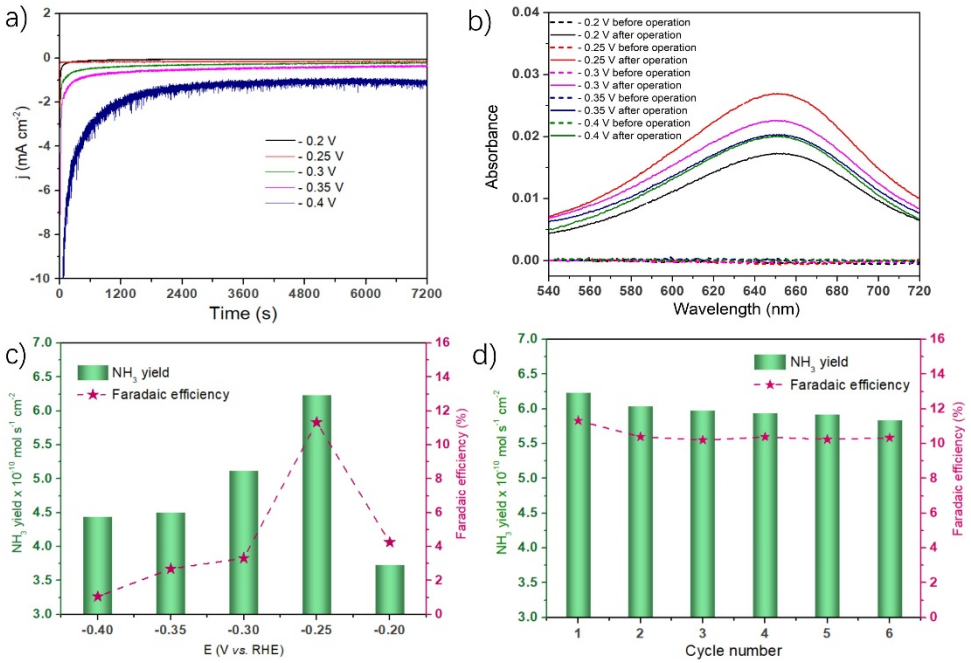

Figure 4 Electrocatalytic NRR on SnO_2@CC electrode and corresponding ammonia production performance. (a) NRR conducted at different potentials. (b) UV adsorption spectra at different potentials before and after the cell operation. (c) Ammonia production performance at various potentials. (d) Examination of cyclic stability (a retention rate of 93%).